Topological surface states and phase transition in $BaTh_2Fe_4As_4(N_{1-x}O_x)_2$ superconductors

Guangwei Wang, Pengyu Zheng, Huican Mao, Yiran Peng, and Zhiping Yin*
Department of Physics and Center for Advanced Quantum Studies, Beijing Normal University, Beijing 100875, China

(Received 7 March 2023; accepted 18 May 2023; published 30 May 2023)

We perform density functional theory and density functional theory plus dynamical mean-field theory calculations to study the electronic structures and topological properties of iron-based superconductors $BaTh_2Fe_4As_4(N_{1-x}O_x)_2$ ($x = 0.1$, 0.2, and 0.3). Taking into account electronic correlation corrections, we find that at small oxygen dopings ($x = 0.1$ and 0.2), the $BaTh_2Fe_4As_4(N_{1-x}O_x)_2$ superconductors have nontrivial band topology and Dirac-cone type topological surface states around the Fermi level on the (001) surface, which indicates that they can harbor Majorana zero modes on the (001) surface. Increasing the oxygen doping level, the $BaTh_2Fe_4As_4(N_{1-x}O_x)_2$ superconductor undergoes a topological phase transition between $x = 0.2$ and 0.3, and has trivial band topology and no topological surface states on the (001) surface at $x = 0.3$. The coexistence of high-temperature superconductivity, topological surface states, and topological phase transition in $BaTh_2Fe_4As_4(N_{1-x}O_x)_2$ superconductors makes them potential platforms to study topological superconductivity, Majorana zero modes and effects induced by a topological phase transition.

DOI: 10.1103/PhysRevB.107.205152

I. INTRODUCTION

Searching for topological superconductors is a research hotspot in condensed matter physics. Topological superconducting states can host Majorana zero modes (MZMs) [1,2], which obey non-Abelian statistics and are expected to be used to realize topological quantum computation [3,4]. However, intrinsic topological superconductors are very rare in nature [5,6]. An alternative way is to construct artificial topological superconductors through the proximity effect, such as atomic chains, semiconductor nanowires, and topological insulator-superconductor heterostructures [7–17]. However, the preparation and manipulation of interfacial structure are too complicated, and the requirement for a long superconducting coherence length hinders the utilization of high-temperature superconductors like cuprate and iron-based superconductors for constructing the artificial heterostructures. A more attractive way for realizing MZMs is to find superconductors with nontrivial band topology and topological surface states in a single material platform [18–30], referred to as connate topological superconductors [23,28,31], thus the complexity and difficulty of interfacial structure is readily avoided.

Thanks to the coexistence of high-temperature superconductivity and nontrivial band topology, iron-based superconductors emerge as a promising single material platform for realizing MZMs in recent years [31,32]. In two-dimensional materials, nontrivial band topology can be induced by a band inversion at the M (Γ) point of the first Brillouin zone (BZ) in monolayer FeSe [22,33] ($FeTe_{1-x}Se_x/SrTiO_3$ [23,34]). In bulk materials, including $FeTe_{0.55}Se_{0.45}$ [24,34–37], Li(Fe,Co)As [26], $(Li_{0.84}Fe_{0.16})OHFeSe$ [25] and $CaKFe_4As_4$ [27], topologically nontrivial band inversions along the $\Gamma-Z$ path of the first BZ give rise to the odd Z_2 invariant and Dirac-cone type topological surface states on the (001) surface, which were confirmed by both first-principles calculations and angle-resolved photoemission spectroscopy experiments. Meanwhile, the signatures of MZMs in these iron-based superconductors were detected through scanning tunneling microscopy/spectroscopy measurements [25,27,38–46]. Layered structure that is easy to cleave, extensive material library, and high-temperature superconductivity make iron-based superconductors a more advantageous single material platform for achieving MZMs. Therefore, it is interesting to find more iron-based superconductors with nontrivial topological properties.

$BaTh_2Fe_4As_4(N_{1-x}O_x)_2$ [47] is an electron-doped 12442-type iron-based superconductor resulting from intergrowth of 122-type $BaFe_2As_2$ [48] and 1111-type $ThFeAsN_{1-x}O_x$ [49]. It is stabilized by the inter-block-layer charge transfer and contains double Fe_2As_2 layers seperated by $Th_2(N_{1-x}O_x)_2$ layers, crystallizing in the body-centered tetragonal lattice with space group $I4/mmm$ (#139). For samples of $0.1 \leqslant x \leqslant 0.7$, the $BaTh_2Fe_4As_4(N_{1-x}O_x)_2$ series have superconducting transition temperature (T_c^{onset}) ranging from 30 to 35 K, and the bulk superconductivity in the solids was confirmed for $0.2 \leqslant x \leqslant 0.6$ with T_c^{bulk} from 20 to 26 K [47]. To our best knowledge, the topological properties of these superconductors have not been reported.

It is well known that electronic correlations have a prominent effect on the electronic structures of iron-based superconductors. The combination of density functional theory [50,51] and dynamical mean-field theory (DFT+DMFT) [52,53] has been proved to be competent for electronic structure calculations of these materials [54–58]. In the studies of topological properties of $(Li_{0.84}Fe_{0.16})OHFeSe$ [25] and $CaKFe_4As_4$ [27], the DFT+DMFT calculated results are in good agreements with experiments. Furthermore, it is

*yinzhiping@bnu.edu.cn

demonstrated by a recent study [59] that electronic correlations play a crucial role in determining the band topology and topological surface states of iron-based superconductors.

In this paper, we carry out DFT and DFT+DMFT calculations to study the electronic structures of $BaTh_2Fe_4As_4(N_{1-x}O_x)_2$ for $x = 0.1$, 0.2, and 0.3, and focus on the band topology and topological surface states. We find that $BaTh_2Fe_4As_4(N_{1-x}O_x)_2$ superconductors are in a topologically nontrivial phase at low doping of $x = 0.1$ and 0.2 and exhibit Dirac-cone type topological surface states near the Fermi level on the (001) surface. The nontrivial band topology is due to the band inversion near the Fermi energy along the $\Gamma-Z$ path between the strongly dispersive As $4p_z$ band and an Fe $3d_{xz}/3d_{yz}$ band which have opposite parity along the $\Gamma-Z$ path at the same time, giving rise to a nontrivial Z_2 topological invariant defined for the bands below a Fermi curve through the spin-orbit coupling (SOC) gap between the above two bands. We also find that $BaTh_2Fe_4As_4(N_{1-x}O_x)_2$ undergoes a topological phase transition between $x = 0.2$ and 0.3 and becomes topologically trivial at $x = 0.3$ when electronic correlation is taken into account, which removes the aforementioned band inversion. Moreover, it is shown that electronic correlation makes the topological surface states on the (001) surface much closer to the Fermi energy, which is good for realizing topological superconducting states and MZMs.

II. COMPUTATIONAL METHOD

The electronic structures of $BaTh_2Fe_4As_4(N_{1-x}O_x)_2$ for $x = 0.1$, 0.2, and 0.3 are calculated by the DFT [50,51] with the Perdew-Burke-Ernzerhof (PBE) form of the generalized gradient approximation as the exchange-correlation potential [60]. We employ two DFT implementations for double checking the results: the Vienna *ab initio* simulation package [61,62] based on the pseudopotential projector augmented wave method and the WIEN2K package [63] based on the full-potential linear augmented plane wave method. Both packages yield convergent results which are in good agreement with each other. The experimental structural parameters [47] are used in the calculations. We apply the virtual crystal approximation to treat the oxygen substitution of nitrogen.

To take into account the strong electronic correlations of Fe $3d$ electrons, we use DFT+DMFT [52,53,64] to calculate the correlated band structures of $BaTh_2Fe_4As_4(N_{1-x}O_x)_2$ ($x = 0.1$, 0.2, and 0.3). The DFT part is based on WIEN2K with the PBE exchange-correlation potential. A Hubbard $U = 5.0$ eV and Hund's coupling $J = 0.8$ eV are used in the DFT+DMFT calculations, in consistency with previous studies [55,56,58,65]. The DMFT quantum impurity problem is solved using the continuous-time quantum Monte Carlo method [66,67] at a temperature of $T = 116$ K. All DFT+DMFT (DFT) calculations are performed in the paramagnetic (nonmagnetic) state. The SOC is included in both the DFT and DFT+DMFT calculations when indicated explicitly.

In order to calculate the surface states on the (001) surface of these materials, tight-binding Hamiltonians based on the maximally localized Wannier functions [68] are constructed using the WANNIER90 code [69] from the DFT band structures. The DFT tight-binding hopping parameters are renormalized to reproduce the DFT+DMFT band structure around the Fermi level through a systematic optimization procedure in order to obtain the DFT+DMFT tight-binding Hamiltonian. The surface spectral functions are calculated by the iterative Green's function method [70] implemented in the WANNIERTOOLS package [71] using both the DFT and DFT+DMFT tight-binding Hamiltonians.

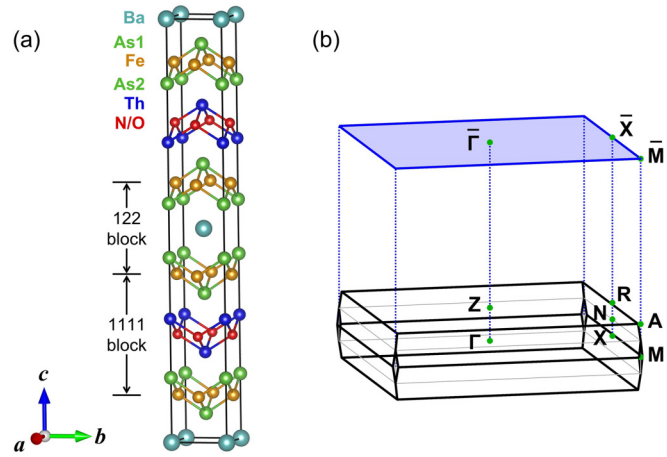

FIG. 1. Crystal structure and Brillouin zone (BZ) of $BaTh_2Fe_4As_4(N_{1-x}O_x)_2$ with space group $I4/mmm$ (#139). (a) Crystal structure. (b) First BZ of the bulk material and its projection on the (001) surface. The relevant high-symmetry points are marked with green dots: Γ (0, 0, 0), X (0.25, −0.25, 0.25), M (0, 0, 0.5), Z (0.5, 0.5, −0.5), R (0.75, 0.25, −0.25), A (0.5, 0.5, 0), and N (0.5, 0, 0). The reciprocal points are given as linear combinations of the basis vectors of the primitive reciprocal lattice.

III. RESULTS AND DISCUSSION

$BaTh_2Fe_4As_4(N_{1-x}O_x)_2$ crystallize in a body-centered tetragonal lattice with space group $I4/mmm$ (No. 139), in which the 122-type $BaFe_2As_2$ and 1111-type $ThFeAsN_{1-x}O_x$ blocks sharing the same Fe planes alternately stack along the c axis as shown in Fig. 1(a). There are two inequivalent arsenic sites (denoted as As1 and As2), adjacent to Ba and $Th_2(N_{1-x}O_x)_2$ layers, respectively. The first BZ of the bulk material and its projection on the (001) surface with the relevant high-symmetry points are shown in Fig. 1(b).

A. Electronic band structures, band topology and nontrivial Z_2 invariant

We first take the system with $x = 0.2$ to illustrate the electronic band structures and topological properties. Figure 2 shows the band structures and Fig. 3 zooms in on the band characters along the $\Gamma-Z$ path combined with the irreducible representations. As shown in the DFT and DFT+DMFT calculated band structures without SOC in Figs. 2(a) and 2(c), double sets of Fe $3d$ t_{2g} bands constitute the dominant states near the Fermi energy. The weakly dispersive bands along the $\Gamma-Z$ path are composed of two sets of twofold degenerate Fe $3d_{xz}/3d_{yz}$ bands and two sets of nondegenerate Fe $3d_{xy}$ bands. Electronic correlations strongly renormalize the DFT bands

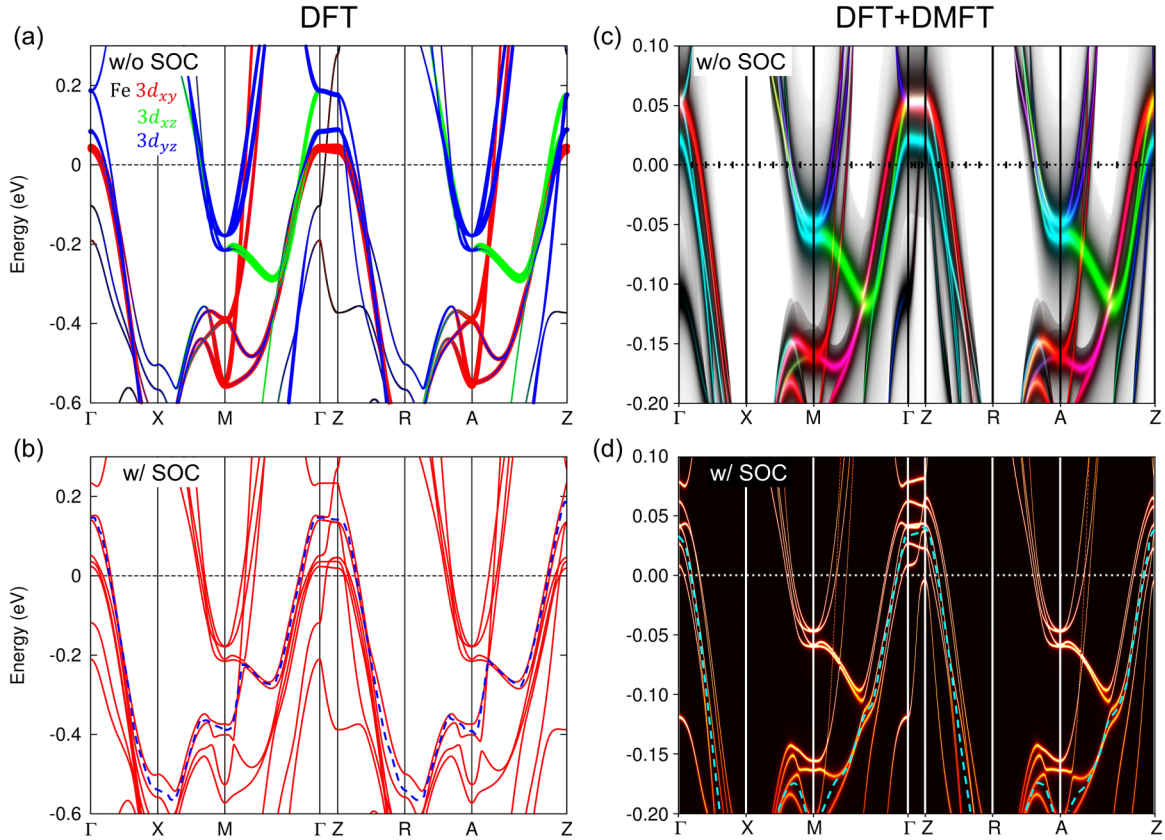

FIG. 2. DFT (left column) and DFT+DMFT (right column) electronic band structures of $BaTh_2Fe_4As_4(N_{0.8}O_{0.2})_2$. (a) DFT and (c) DFT+DMFT Fe $3d_{xy}$ (red), $3d_{xz}$ (green), and $3d_{yz}$ (blue) orbital-resolved band structures without (w/o) SOC. (b) DFT and (d) DFT+DMFT band structures with (w/) SOC. In panels (b) and (d), the blue and cyan dashed lines correspond to the Fermi curve through the SOC gap.

of Fe $3d$ electrons by a factor of $3 \sim 4$. Along the $\Gamma-Z$ path, the two Fe $3d_{xy}$ bands are below the two sets of Fe $3d_{xz}/3d_{yz}$ bands in DFT, whereas the two Fe $3d_{xy}$ bands locate close to the higher-energy Fe $3d_{xz}/3d_{yz}$ bands in DFT+DMFT. The strongly dispersive band across the Fermi level along the $\Gamma-Z$ path mainly derives from the $4p_z$ orbital of As2 hybridizing with Fe $3d_{z^2}$ orbital and N/O $2p_z$ orbital, as shown in Fig. 3(a) and Fig. S1 [72].

As shown in Figs. 3(c) and 3(e), the higher (lower) twofold degenerate Fe $3d_{xz}/3d_{yz}$ bands belong to the Γ_5^- (Γ_5^+) irreducible representation at both the Γ and Z points, while the higher (lower) nondegenerate Fe $3d_{xy}$ band belongs to the Γ_4^- (Γ_3^+) representation. The As2 $4p_z$ dominated band which intersects the Fe $3d$ t_{2g} bands and the Fermi level along the $\Gamma-Z$ path is labeled as Γ_1^+ state. It is noted that there is an exchange of band order between the Γ_1^+ state (As2 $4p_z$ orbital) and the Γ_2^- state (Fe $3d_{z^2}$ state) at the Γ point, as illustrated in Fig. 3(a). When SOC is included, the doubly degenerate Γ_5^- (Γ_5^+) states split into Γ_6^- and Γ_7^- (Γ_6^+ and Γ_7^+), the nondegenerate Γ_4^- (Γ_3^+) state becomes Γ_7^- (Γ_7^+), and the Γ_1^+ state turns into Γ_6^+, as shown in Figs. 3(d) and 3(f). Along the $\Gamma-Z$ path, the strongly dispersive Γ_6^+ band and both the weakly dispersive Γ_6^- and Γ_6^+ bands have the same Λ_6 irreducible representation under C_{4v} symmetry, which leads to band anticrossing and SOC gap opening. Notably, the band inversion between the odd-parity Γ_6^- band and the strongly dispersive even-parity Γ_6^+ band [indicated by the green dashed circle in Figs. 3(d) and 3(f)] drives the system into a topologically nontrivial phase due to the accompanying parity exchange.

To firmly confirm the topological nature related to the band inversion between the Γ_6^- band and the strongly dispersive Γ_6^+ band, one can assume a "curved chemical potential" (Fermi curve) [35] through the continuous direct SOC gap to define Z_2 topological invariants [73–75], as shown by the blue (cyan) dashed lines in Figs. 3(d) and 3(f) [also in Figs. 2(b) and 2(d)]. Thanks to the presence of three-dimensional inversion symmetry in $BaTh_2Fe_4As_4(N_{1-x}O_x)_2$, we can calculate Z_2 topological invariants by the Fu-Kane parity criterion [76] from the knowledge of the wavefunction parities of all the bands below the Fermi curve at the eight time-reversal invariant momenta points in the first BZ. The Z_2 invariant $\nu_0 = 0, 1$, which distinguishes the strong topological insulator in three dimensions, is given by the product over all eight points $(-1)^{\nu_0} = \prod_{i=1}^{8} \delta_i$, where δ_i is the product of wavefunction parities of all the bands below the Fermi curve at the ith time-reversal invariant momentum point. Among the eight time-reversal invariant momenta points in the first BZ of $BaTh_2Fe_4As_4(N_{1-x}O_x)_2$ with space group $I4/mmm$, there are four equivalent points denoted by N and two equivalent points denoted by A/M, so the parity product over these six points is always 1. Therefore, only the parity products at the

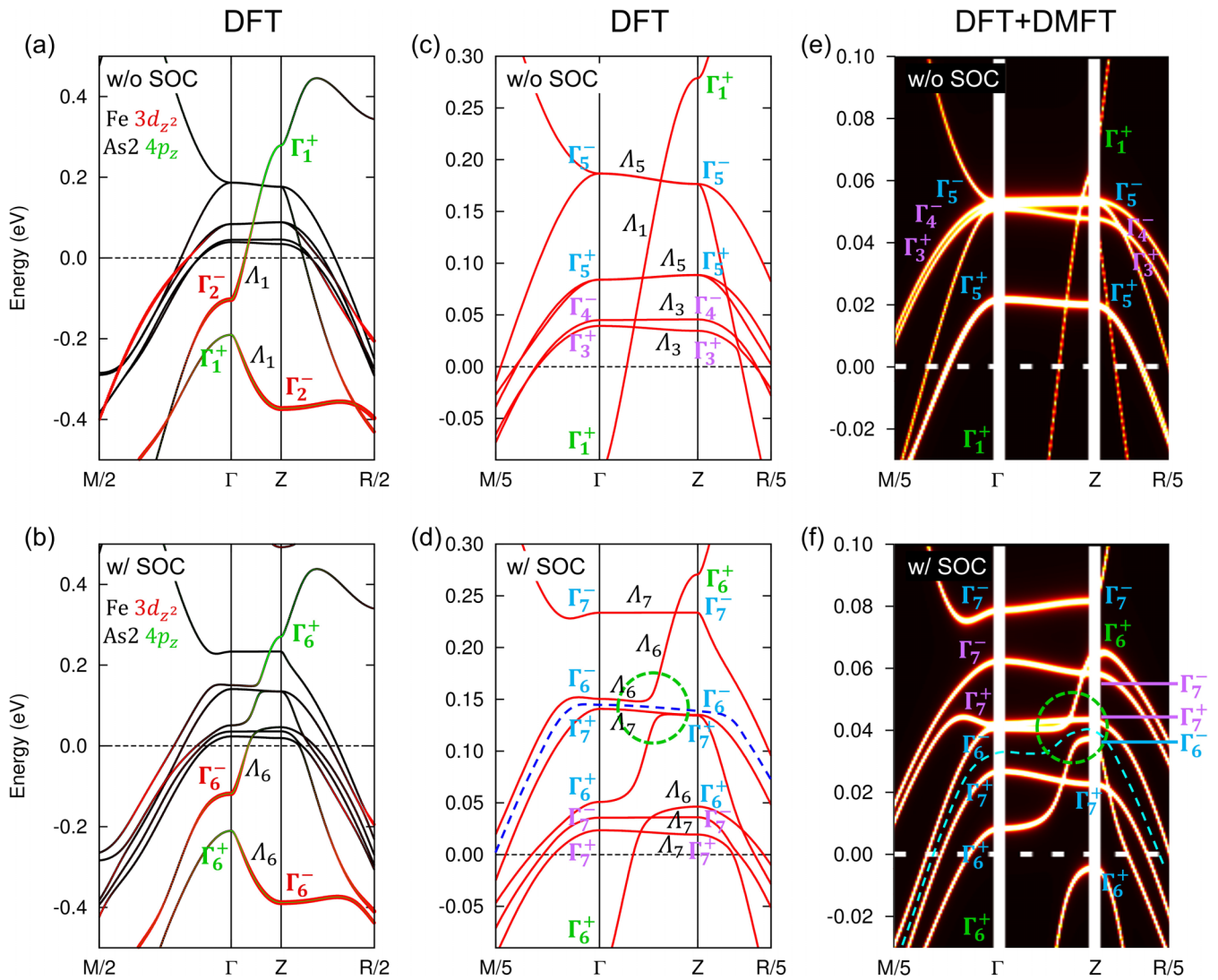

FIG. 3. DFT (a)–(d) and DFT+DMFT (e), (f) band topology along the $\Gamma-Z$ path of $BaTh_2Fe_4As_4(N_{0.8}O_{0.2})_2$. DFT band structure with Fe $3d_{z^2}$ and As2 $4p_z$ orbital projections and the irreducible representations of the projected states along the $\Gamma-Z$ path without (a) and with (b) SOC. Irreducible representations of the bands near the Fermi energy along the $\Gamma-Z$ path in the DFT (c), (d) and DFT+DMFT (e), (f) band structures without (c), (e) and with (d), (f) SOC. In panels (d) and (f), the green dashed circle indicates the band inversion and the SOC gap between the odd-parity Γ_6^- band and the strongly dispersive even-parity Γ_6^+ band that gives rise to the nontrivial Z_2 topological invariant. The blue (d) and cyan (f) dashed lines correspond to the Fermi curve through the SOC gap.

Γ and Z points are needed to determine ν_0. The parities at these two points of the DFT calculated band structure are detailed in Fig. S2 [72]. It is clearly shown that the parity exchange brought by the band inversion between the Γ_6^- band and the strongly dispersive Γ_6^+ band leads to negative parity product of the bands below the Fermi curve over both the Γ and Z points. Consequently, the Z_2 invariant ν_0 comes out to 1, indicating that the material is in a nontrivial topological phase. In the DFT+DMFT calculated band structure, the relative energy positions of the Fe $3d_{xy}$ and $3d_{xz}/3d_{yz}$ bands are renormalized and shifted, which can be seen in Figs. 2(a) and 2(c) and Figs. 3(c) and 3(e). As a result, in comparison with their DFT counterparts, a pair of $\Gamma_7^{\pm}$ bands are shifted above the Fermi curve at both Γ and Z points in the band structure with SOC as displayed in Fig. 3(f), which does not change the parity product of the bands below the Fermi curve over both the Γ and Z points. Therefore, the material remains topologically nontrivial after considering strong electronic correlation effects on the band structure.

B. Topological phase transition by tuning the doping level

Besides $x = 0.2$, we also investigate the band structures and topological properties at other doping levels $x = 0.1$ and $x = 0.3$. As discussed above, the key ingredient driving the topologically nontrivial phase is the band inversion between the Γ_6^- band and the strongly dispersive Γ_6^+ band along the $\Gamma-Z$ path. For simplicity, we only plot the band structures without SOC calculated by both DFT and DFT+DMFT for three doping concentrations in Fig. 4. We find that the odd Γ_5^- band from which the odd Γ_6^- band originates (Fig. 3) only slightly changes with increasing doping level. As a result, we focus mainly on the strongly dispersive Γ_6^+ band dominated

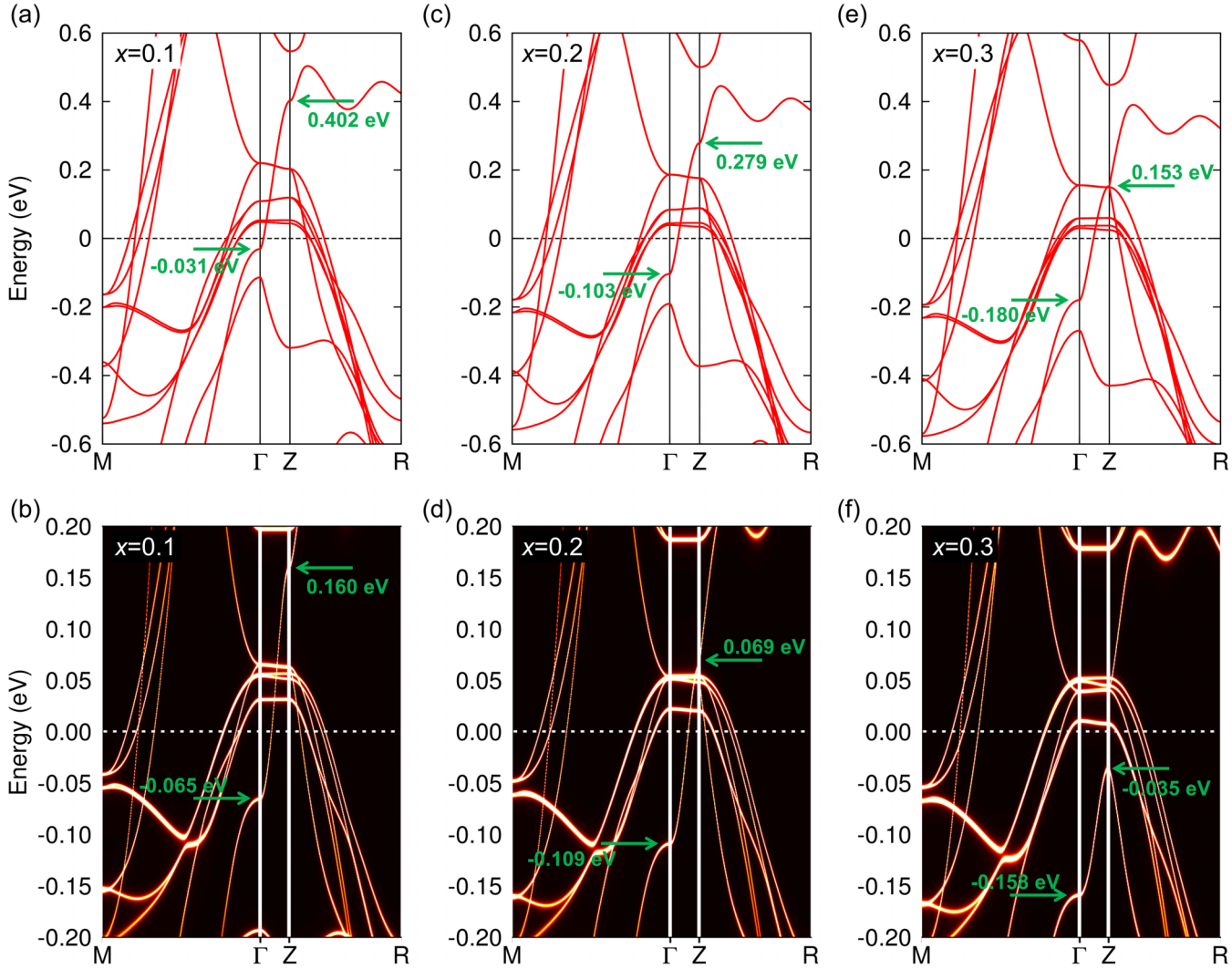

FIG. 4. DFT (top row) and DFT+DMFT (bottom row) electronic band structures without SOC of $BaTh_2Fe_4As_4(N_{1-x}O_x)_2$ for $x = 0.1$ (a), (b), 0.2 (c), (d), and 0.3 (e), (f). In each panel, the arrows indicate the energy positions at both Γ and Z points of the strongly dispersive band along the $\Gamma-Z$ path.

by As2 $4p_z$ orbital along the $\Gamma-Z$ path in the following analysis.

As can be seen in Fig. 4, increasing the doping level from $x = 0.1$ to 0.3, the strongly dispersive Γ_6^+ band is moved downward noticeably along the $\Gamma-Z$ path in both DFT and DFT+DMFT calculations. In particular, the energy position of this band at the Z point is shifted down by ∼0.25 eV and 0.20 eV in DFT and DFT+DMFT calculations, respectively, as the doping concentration is increased from $x = 0.1$ to 0.3. Moreover, compared to the DFT results at the same doping level for $x = 0.1$, 0.2, and 0.3, the DFT+DMFT band width of this strongly dispersive band along the $\Gamma-Z$ path is compressed by a factor of ∼1.9, 2.2, and 2.7, while the band energy at the Z point is lowered by ∼0.24 eV, 0.21 eV, and 0.19 eV, respectively.

For $x = 0.1$, both DFT and DFT+DMFT band structures exhibit the key band inversion (Fig. S4) [72] similar to $x = 0.2$ as discussed above. Therefore, we can define a Fermi curve through the SOC gap between the Fe $3d_{xz}/3d_{yz}$ band and the strongly dispersive Γ_6^+ band along the $\Gamma-Z$ path and obtain a nontrivial Z_2 topological invariant for all the bands below the Fermi curve as shown in Figs. 5(a) and 5(c). However, for $x = 0.3$, while this band inversion is still present in DFT calculations [Fig. 5(b)], it vanishes in DFT+DMFT calculations [Fig. 5(d)] after strong electronic correlation is considered which significantly lowers the strongly dispersive As2 $4p_z$ band along the $\Gamma-Z$ path such that it no longer crosses the Fe $3d_{xz}/3d_{yz}$ bands. Therefore, a topological phase transition is induced by electronic correlation at a doping between $x = 0.2$ and 0.3. Our study suggests that both doping and electronic correlation are effective ways to induce topological phase transitions in correlated topological materials.

C. Topological surface states

A direct consequence of a nontrivial Z_2 topological invariant is the existence of topological surface states. As shown in Figs. 6(a)–6(d), it is found that there are Dirac-cone type topological surface states on the (001) surface for $x = 0.1$ and 0.2 in both DFT and DFT+DMFT calculations. The energy

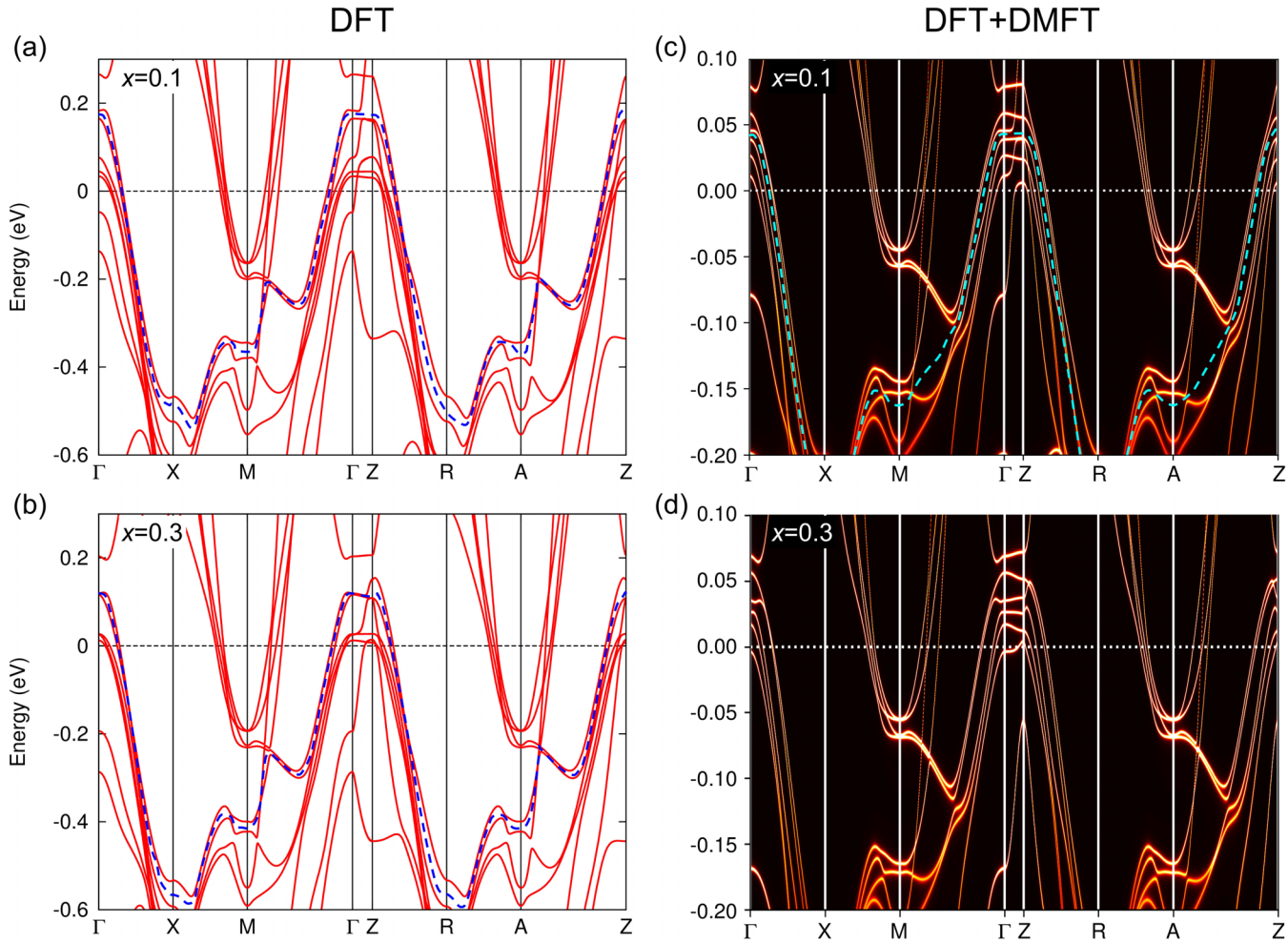

FIG. 5. DFT (left column) and DFT+DMFT (right column) electronic band structures with SOC of $BaTh_2Fe_4As_4(N_{1-x}O_x)_2$ for $x = 0.1$ (a), (c) and 0.3 (b), (d). In panels (a), (b), and (c), the blue and cyan dashed lines correspond to the Fermi curve through the SOC gap.

position of the center of the Dirac-cone surface states is mainly determined by the odd Γ_6^- band. With increasing doping level, the Fermi energy is increased thus the odd Γ_6^- band along the $\Gamma-Z$ path gets closer to the Fermi level, which makes the center of the topological surface states on the (001) surface closer to the Fermi energy, as shown in Figs. 6(a) and 6(c) and Figs. 6(b) and 6(d) for DFT and DFT+DMFT calculations, respectively. For $x = 0.3$, the topological surface states only exist in DFT but not in DFT+DMFT [Figs. 6(e) and 6(f)] due to the absence of the band inversion in DFT+DMFT, which confirms that the material becomes topologically trivial at $x = 0.3$ when electronic correlation is taken into account. Moreover, by comparing the energy positions of the topological surfaces states in DFT and DFT+DMFT calculations, we find that electronic correlations move the topological surface states much closer to the Fermi energy [59], which is favorable for further experimental observation and the realization of topological superconducting states and MZMs.

IV. CONCLUSIONS

In conclusion, we present DFT and DFT+DMFT calculations of $BaTh_2Fe_4As_4(N_{1-x}O_x)_2$ ($x = 0.1$, 0.2, and 0.3) superconductors and systematically study their band structures and topological properties. When electronic correlation is properly taken into account as in DFT+DMFT calculations, we find that these superconductors are in a topologically nontrivial phase at low doping levels ($x = 0.1$ and 0.2), which is due to the band inversion and opposite parity between the Fe $3d_{xz}/3d_{yz}$ Γ_6^- band and the strongly dispersive As2 $4p_z$ Γ_6^+ band along the $\Gamma-Z$ path. As a result, Dirac-cone type topological surface states emerge near the Fermi level on the (001) surface. When doping is further increased, the strongly dispersive As2 $4p_z$ band along the $\Gamma-Z$ path is rapidly lowered by both doping and electronic correlation effects. At $x = 0.3$, the strongly dispersive As2 $4p_z$ band is below the Fe $3d_{xz}/3d_{yz}$ bands along the $\Gamma-Z$ path, hence the aforementioned band inversion vanishes, which makes the system topologically trivial and no longer have topological surface states on the (001) surface. Therefore, a topological phase transition occurs between $x = 0.2$ and 0.3. Considering the coexistence of both superconductivity and topological surface states at $x = 0.1$ and 0.2 and the topological phase transition between $x = 0.2$ and 0.3, our findings suggest that the $BaTh_2Fe_4As_4(N_{1-x}O_x)_2$ superconductor family has the potential to be a good platform to realize topological superconductivity and MZMs and

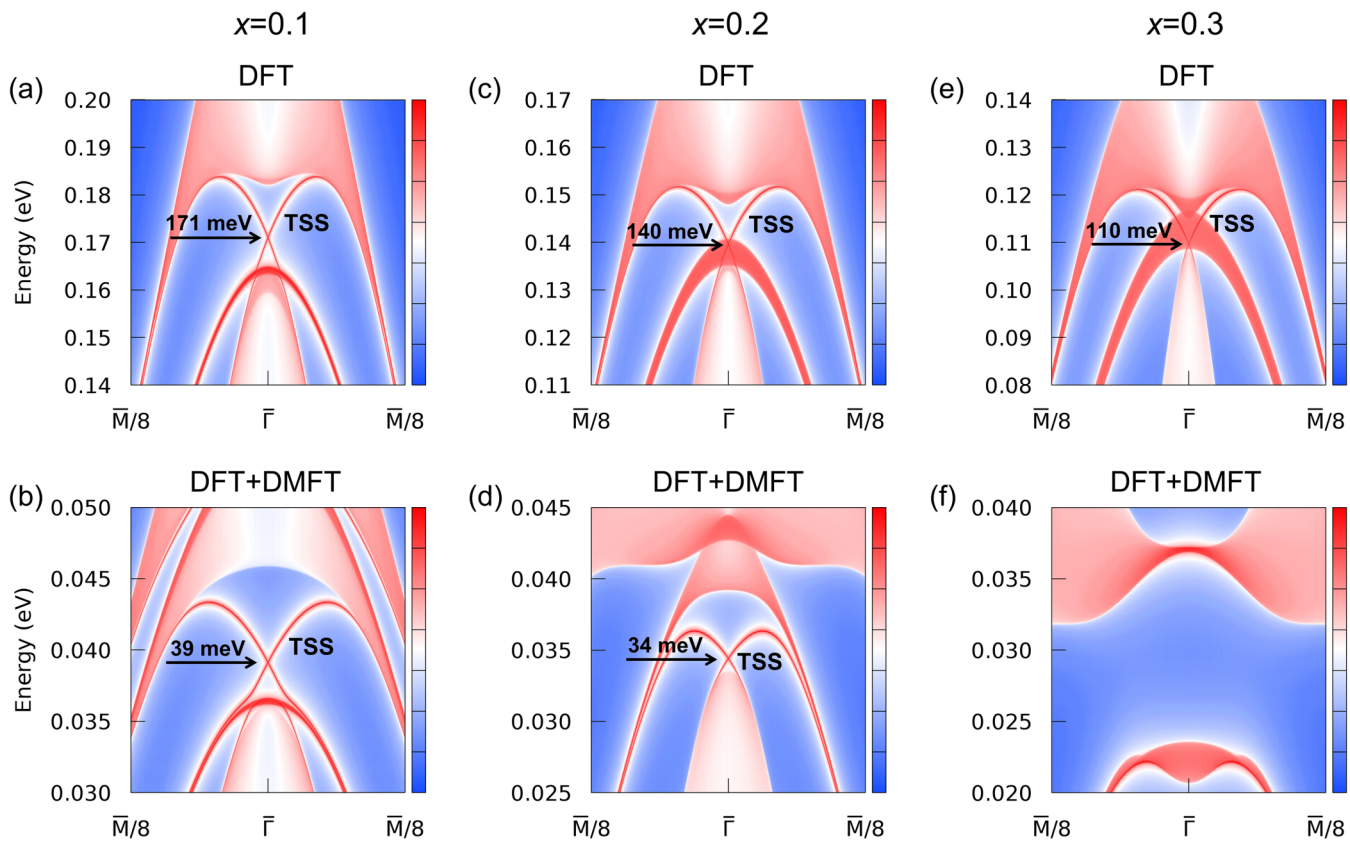

FIG. 6. DFT (top row) and DFT+DMFT (bottom row) surface states of $BaTh_2Fe_4As_4(N_{1-x}O_x)_2$ ($x = 0.1$, 0.2, and 0.3) on the (001) surface. In each panel, the arrow indicates the energy position of the Dirac point of the topological surface state (TSS) centered at $\bar{\Gamma}$ point. There is no topological surface state in panel (f).

to explore the effects of topological phase transition in a superconductor.

ACKNOWLEDGMENTS

This work was supported by the National Natural Science Foundation of China (Grants No. 12074041 and No. 11674030), the Foundation of the National Key Laboratory of Shock Wave and Detonation Physics (Grant No. 6142A03191005), the National Key Research and Development Program of China through Contract No. 2016YFA0302300, and the startup funding of Beijing Normal University. The calculations were carried out with high performance computing cluster of Beijing Normal University in Zhuhai.

[1] X.-L. Qi and S.-C. Zhang, Rev. Mod. Phys. **83**, 1057 (2011).
[2] M. Sato and Y. Ando, Rep. Prog. Phys. **80**, 076501 (2017).
[3] C. Nayak, S. H. Simon, A. Stern, M. Freedman, and S. Das Sarma, Rev. Mod. Phys. **80**, 1083 (2008).
[4] C. Beenakker, Annu. Rev. Condens. Matter Phys. **4**, 113 (2013).
[5] C. Kallin, Rep. Prog. Phys. **75**, 042501 (2012).
[6] N. Levy, T. Zhang, J. Ha, F. Sharifi, A. A. Talin, Y. Kuk, and J. A. Stroscio, Phys. Rev. Lett. **110**, 117001 (2013).
[7] J. Alicea, Rep. Prog. Phys. **75**, 076501 (2012).
[8] S. Nadj-Perge, I. K. Drozdov, J. Li, H. Chen, S. Jeon, J. Seo, A. H. MacDonald, B. A. Bernevig, and A. Yazdani, Science **346**, 602 (2014).
[9] M. Ruby, F. Pientka, Y. Peng, F. von Oppen, B. W. Heinrich, and K. J. Franke, Phys. Rev. Lett. **115**, 197204 (2015).
[10] R. M. Lutchyn, J. D. Sau, and S. Das Sarma, Phys. Rev. Lett. **105**, 077001 (2010).
[11] V. Mourik, K. Zuo, S. M. Frolov, S. R. Plissard, E. P. A. M. Bakkers, and L. P. Kouwenhoven, Science **336**, 1003 (2012).
[12] S. M. Albrecht, A. P. Higginbotham, M. Madsen, F. Kuemmeth, T. S. Jespersen, J. Nygård, P. Krogstrup, and C. M. Marcus, Nature (London) **531**, 206 (2016).
[13] S. Manna, P. Wei, Y. Xie, K. T. Law, P. A. Lee, and J. S. Moodera, Proc. Natl. Acad. Sci. USA **117**, 8775 (2020).
[14] L. Fu and C. L. Kane, Phys. Rev. Lett. **100**, 096407 (2008).
[15] M.-X. Wang, C. Liu, J.-P. Xu, F. Yang, L. Miao, M.-Y. Yao, C. L. Gao, C. Shen, X. Ma, X. Chen, Z.-A. Xu, Y. Liu, S.-C. Zhang, D. Qian, J.-F. Jia, and Q.-K. Xue, Science **336**, 52 (2012).
[16] J.-P. Xu, C. Liu, M.-X. Wang, J. Ge, Z.-L. Liu, X. Yang, Y. Chen, Y. Liu, Z.-A. Xu, C.-L. Gao, D. Qian, F.-C. Zhang, and J.-F. Jia, Phys. Rev. Lett. **112**, 217001 (2014).

[17] H.-H. Sun, K.-W. Zhang, L.-H. Hu, C. Li, G.-Y. Wang, H.-Y. Ma, Z.-A. Xu, C.-L. Gao, D.-D. Guan, Y.-Y. Li, C. Liu, D. Qian, Y. Zhou, L. Fu, S.-C. Li, F.-C. Zhang, and J.-F. Jia, Phys. Rev. Lett. **116**, 257003 (2016).
[18] S.-Y. Guan, P.-J. Chen, M.-W. Chu, R. Sankar, F. Chou, H.-T. Jeng, C.-S. Chang, and T.-M. Chuang, Sci. Adv. **2**, e1600894 (2016).
[19] T. Le, Y. Sun, H.-K. Jin, L. Che, L. Yin, J. Li, G. Pang, C. Xu, L. Zhao, S. Kittaka, T. Sakakibara, K. Machida, R. Sankar, H. Yuan, G. Chen, X. Xu, S. Li, Y. Zhou, and X. Lu, Sci. Bull. **65**, 1349 (2020).
[20] Y. Fang, J. Pan, D. Zhang, D. Wang, H. T. Hirose, T. Terashima, S. Uji, Y. Yuan, W. Li, Z. Tian, J. Xue, Y. Ma, W. Zhao, Q. Xue, G. Mu, H. Zhang, and F. Huang, Adv. Mater. **31**, 1901942 (2019).
[21] Y. Yuan, J. Pan, X. Wang, Y. Fang, C. Song, L. Wang, K. He, X. Ma, H. Zhang, F. Huang, W. Li, and Q.-K. Xue, Nat. Phys. **15**, 1046 (2019).
[22] Z. F. Wang, H. Zhang, D. Liu, C. Liu, C. Tang, C. Song, Y. Zhong, J. Peng, F. Li, C. Nie, L. Wang, X. J. Zhou, X. Ma, Q. K. Xue, and F. Liu, Nat. Mater. **15**, 968 (2016).
[23] X. Shi, Z.-Q. Han, P. Richard, X.-X. Wu, X.-L. Peng, T. Qian, S.-C. Wang, J.-P. Hu, Y.-J. Sun, and H. Ding, Sci. Bull. **62**, 503 (2017).
[24] P. Zhang, K. Yaji, T. Hashimoto, Y. Ota, T. Kondo, K. Okazaki, Z. Wang, J. Wen, G. D. Gu, H. Ding, and S. Shin, Science **360**, 182 (2018).
[25] Q. Liu, C. Chen, T. Zhang, R. Peng, Y.-J. Yan, C.-H.-P. Wen, X. Lou, Y.-L. Huang, J.-P. Tian, X.-L. Dong, G.-W. Wang, W.-C. Bao, Q.-H. Wang, Z.-P. Yin, Z.-X. Zhao, and D.-L. Feng, Phys. Rev. X **8**, 041056 (2018).
[26] P. Zhang, Z. Wang, X. Wu, K. Yaji, Y. Ishida, Y. Kohama, G. Dai, Y. Sun, C. Bareille, K. Kuroda, T. Kondo, K. Okazaki, K. Kindo, X. Wang, C. Jin, J. Hu, R. Thomale, K. Sumida, S. Wu, K. Miyamoto *et al.*, Nat. Phys. **15**, 41 (2019).
[27] W. Liu, L. Cao, S. Zhu, L. Kong, G. Wang, M. Papaj, P. Zhang, Y.-B. Liu, H. Chen, G. Li, F. Yang, T. Kondo, S. Du, G.-H. Cao, S. Shin, L. Fu, Z. Yin, H.-J. Gao, and H. Ding, Nat. Commun. **11**, 5688 (2020).
[28] J.-Y. Guan, L. Kong, L.-Q. Zhou, Y.-G. Zhong, H. Li, H.-J. Liu, C.-Y. Tang, D.-Y. Yan, F.-Z. Yang, Y.-B. Huang, Y.-G. Shi, T. Qian, H.-M. Weng, Y.-J. Sun, and H. Ding, Sci. Bull. **64**, 1215 (2019).
[29] S. Nie, L. Xing, R. Jin, W. Xie, Z. Wang, and F. B. Prinz, Phys. Rev. B **98**, 125143 (2018).
[30] C. Chen, A. Liang, S. Liu, S. Nie, J. Huang, M. Wang, Y. Li, D. Pei, H. Yang, H. Zheng, Y. Zhang, D. Lu, M. Hashimoto, A. Barinov, C. Jozwiak, A. Bostwick, E. Rotenberg, X. Kou, L. Yang, Y. Guo *et al.*, Matter **3**, 2055 (2020).
[31] N. Hao and J. Hu, Natl. Sci. Rev. **6**, 213 (2019).
[32] L. Sang, Z. Li, G. Yang, M. Nadeem, L. Wang, Q. Xue, A. R. Hamilton, and X. Wang, Matter **5**, 1734 (2022).
[33] N. Hao and J. Hu, Phys. Rev. X **4**, 031053 (2014).
[34] X. Wu, S. Qin, Y. Liang, H. Fan, and J. Hu, Phys. Rev. B **93**, 115129 (2016).
[35] Z. Wang, P. Zhang, G. Xu, L. K. Zeng, H. Miao, X. Xu, T. Qian, H. Weng, P. Richard, A. V. Fedorov, H. Ding, X. Dai, and Z. Fang, Phys. Rev. B **92**, 115119 (2015).
[36] G. Xu, B. Lian, P. Tang, X.-L. Qi, and S.-C. Zhang, Phys. Rev. Lett. **117**, 047001 (2016).
[37] H. Lohani, T. Hazra, A. Ribak, Y. Nitzav, H. Fu, B. Yan, M. Randeria, and A. Kanigel, Phys. Rev. B **101**, 245146 (2020).
[38] J.-X. Yin, Z. Wu, J.-H. Wang, Z.-Y. Ye, J. Gong, X.-Y. Hou, L. Shan, A. Li, X.-J. Liang, X.-X. Wu, J. Li, C.-S. Ting, Z.-Q. Wang, J.-P. Hu, P.-H. Hor, H. Ding, and S. H. Pan, Nat. Phys. **11**, 543 (2015).
[39] D. Wang, L. Kong, P. Fan, H. Chen, S. Zhu, W. Liu, L. Cao, Y. Sun, S. Du, J. Schneeloch, R. Zhong, G. Gu, L. Fu, H. Ding, and H.-J. Gao, Science **362**, 333 (2018).
[40] T. Machida, Y. Sun, S. Pyon, S. Takeda, Y. Kohsaka, T. Hanaguri, T. Sasagawa, and T. Tamegai, Nat. Mater. **18**, 811 (2019).
[41] L. Kong, S. Zhu, M. Papaj, H. Chen, L. Cao, H. Isobe, Y. Xing, W. Liu, D. Wang, P. Fan, Y. Sun, S. Du, J. Schneeloch, R. Zhong, G. Gu, L. Fu, H.-J. Gao, and H. Ding, Nat. Phys. **15**, 1181 (2019).
[42] Z. Wang, J. O. Rodriguez, L. Jiao, S. Howard, M. Graham, G. D. Gu, T. L. Hughes, D. K. Morr, and V. Madhavan, Science **367**, 104 (2020).
[43] S. Zhu, L. Kong, L. Cao, H. Chen, M. Papaj, S. Du, Y. Xing, W. Liu, D. Wang, C. Shen, F. Yang, J. Schneeloch, R. Zhong, G. Gu, L. Fu, Y.-Y. Zhang, H. Ding, and H.-J. Gao, Science **367**, 189 (2020).
[44] P. Fan, F. Yang, G. Qian, H. Chen, Y.-Y. Zhang, G. Li, Z. Huang, Y. Xing, L. Kong, W. Liu, K. Jiang, C. Shen, S. Du, J. Schneeloch, R. Zhong, G. Gu, Z. Wang, H. Ding, and H.-J. Gao, Nat. Commun. **12**, 1348 (2021).
[45] L. Kong, L. Cao, S. Zhu, M. Papaj, G. Dai, G. Li, P. Fan, W. Liu, F. Yang, X. Wang, S. Du, C. Jin, L. Fu, H.-J. Gao, and H. Ding, Nat. Commun. **12**, 4146 (2021).
[46] M. Li, G. Li, L. Cao, X. Zhou, X. Wang, C. Jin, C.-K. Chiu, S. J. Pennycook, Z. Wang, and H.-J. Gao, Nature (London) **606**, 890 (2022).
[47] Y.-T. Shao, Z.-C. Wang, B.-Z. Li, S.-Q. Wu, J.-F. Wu, Z. Ren, S.-W. Qiu, C. Rao, C. Wang, and G.-H. Cao, Sci. China Mater. **62**, 1357 (2019).
[48] M. Rotter, M. Tegel, D. Johrendt, I. Schellenberg, W. Hermes, and R. Pöttgen, Phys. Rev. B **78**, 020503(R) (2008).
[49] B.-Z. Li, Z.-C. Wang, J.-L. Wang, F.-X. Zhang, D.-Z. Wang, F.-Y. Zhang, Y.-P. Sun, Q. Jing, H.-F. Zhang, S.-G. Tan, Y.-K. Li, C.-M. Feng, Y.-X. Mei, C. Wang, and G.-H. Cao, J. Phys.: Condens. Matter **30**, 255602 (2018).
[50] P. Hohenberg and W. Kohn, Phys. Rev. **136**, B864 (1964).
[51] W. Kohn and L. J. Sham, Phys. Rev. **140**, A1133 (1965).
[52] A. Georges, G. Kotliar, W. Krauth, and M. J. Rozenberg, Rev. Mod. Phys. **68**, 13 (1996).
[53] G. Kotliar, S. Y. Savrasov, K. Haule, V. S. Oudovenko, O. Parcollet, and C. A. Marianetti, Rev. Mod. Phys. **78**, 865 (2006).
[54] K. Haule, J. H. Shim, and G. Kotliar, Phys. Rev. Lett. **100**, 226402 (2008).
[55] Z. P. Yin, K. Haule, and G. Kotliar, Nat. Phys. **7**, 294 (2011).
[56] Z. P. Yin, K. Haule, and G. Kotliar, Nat. Mater. **10**, 932 (2011).
[57] G. Lee, H. S. Ji, Y. Kim, C. Kim, K. Haule, G. Kotliar, B. Lee, S. Khim, K. H. Kim, K. S. Kim, K.-S. Kim, and J. H. Shim, Phys. Rev. Lett. **109**, 177001 (2012).
[58] Z. P. Yin, K. Haule, and G. Kotliar, Phys. Rev. B **86**, 195141 (2012).
[59] X. Ma, G. Wang, R. Liu, T. Yu, Y. Peng, P. Zheng, and Z. Yin, Phys. Rev. B **106**, 115114 (2022).

[60] J. P. Perdew, K. Burke, and M. Ernzerhof, Phys. Rev. Lett. **77**, 3865 (1996).
[61] G. Kresse and J. Furthmüller, Comput. Mater. Sci. **6**, 15 (1996).
[62] G. Kresse and J. Furthmüller, Phys. Rev. B **54**, 11169 (1996).
[63] P. Blaha, K. Schwarz, G. K. Madsen, D. Kvasnicka, and J. Luitz, WIEN2K, An *Augmented Plane Wave + Local Orbitals Program for Calculating Crystal Properties* (Karlheinz Schwarz, Vienna University of Technology, Austria, 2001).
[64] K. Haule, C.-H. Yee, and K. Kim, Phys. Rev. B **81**, 195107 (2010).
[65] Z. P. Yin, K. Haule, and G. Kotliar, Nat. Phys. **10**, 845 (2014).
[66] P. Werner, A. Comanac, L. de' Medici, M. Troyer, and A. J. Millis, Phys. Rev. Lett. **97**, 076405 (2006).
[67] K. Haule, Phys. Rev. B **75**, 155113 (2007).
[68] N. Marzari, A. A. Mostofi, J. R. Yates, I. Souza, and D. Vanderbilt, Rev. Mod. Phys. **84**, 1419 (2012).
[69] A. A. Mostofi, J. R. Yates, G. Pizzi, Y.-S. Lee, I. Souza, D. Vanderbilt, and N. Marzari, Comput. Phys. Commun. **185**, 2309 (2014).
[70] M. P. L. Sancho, J. M. L. Sancho, J. M. L. Sancho, and J. Rubio, J. Phys. F: Met. Phys. **15**, 851 (1985).
[71] Q. Wu, S. Zhang, H.-F. Song, M. Troyer, and A. A. Soluyanov, Comput. Phys. Commun. **224**, 405 (2018).
[72] See Supplemental Material at http://link.aps.org/supplemental/10.1103/PhysRevB.107.205152 for the N/O $2p_z$ orbital projected band structure, the detailed parity analysis of the DFT band structure of the $x = 0.2$ system, and the analysis of the band topology for the $x = 0.1$ and 0.3 systems.
[73] J. E. Moore and L. Balents, Phys. Rev. B **75**, 121306(R) (2007).
[74] L. Fu, C. L. Kane, and E. J. Mele, Phys. Rev. Lett. **98**, 106803 (2007).
[75] R. Roy, Phys. Rev. B **79**, 195322 (2009).
[76] L. Fu and C. L. Kane, Phys. Rev. B **76**, 045302 (2007).